Key Points:
- Fluorescence difference of cells and stained minerals captured by a full-color μPIV system was used to map cell colonization patterns
- An evolution of three colonization patterns over an increasing biomass fraction suggests a colonization mechanism progress
- Correlations of cell colonization with sucrose concentrations and aggregate geometry were highlighted

Optical Measurement of Cell Colonization Patterns on Individual Suspended Sediment Aggregates

Thu Ha Nguyen[1] (iD)**, Fiona H. M. Tang**[1] (iD)**, and Federico Maggi**[1] (iD)

[1]Laboratory for Advanced Environmental Engineering Research, School of Civil Engineering, The University of Sydney, Sydney, New South Wales, Australia

Abstract Microbial processes can make substantial differences to the way in which particles settle in aquatic environments. A novel method (OMCEC, optical measurement of cell colonization) is introduced to systematically map the biological spatial distribution over individual suspended sediment aggregates settling through a water column. OMCEC was used to investigate (1) whether a carbon source concentration has an impact on cell colonization, (2) how cells colonize minerals, and (3) if a correlation between colonization patterns and aggregate geometry exists. Incubations of *Saccharomyces cerevisiae* and stained montmorillonite at four sucrose concentrations were tested in a settling column equipped with a full-color microparticle image velocimetry system. The acquired high-resolution images were processed to map the cell distribution on aggregates based on emission spectra separation. The likelihood of cells colonizing minerals increased with increasing sucrose concentration. Colonization patterns were classified into (i) scattered, (ii) well touched, and (iii) poorly touched, with the second being predominant. Cell clusters in well-touched patterns were found to have lower capacity dimension than those in other patterns, while the capacity dimension of the corresponding aggregates was relatively high. A strong correlation of colonization patterns with aggregate biomass fraction and properties suggests dynamic colonization mechanisms from cell attachment to minerals, to joining of isolated cell clusters, and finally cell growth over the entire aggregate. This paper introduces a widely applicable method for analyses of microbial-affected sediment dynamics and highlights the microbial control on aggregate geometry, which can improve the prediction of large-scale morphodynamics processes.

1. Introduction

The fate of suspended particulate matter (SPM) plays a vital role in controlling large-scale processes related to geophysical flows such as dispersal and sinking of organic matter and contaminants to offshore and deep waters, nutrient cycles, food web stability, and sediment transport in both limnetic and pelagic ecosystems (e.g., Alldredge & Gotschalk, 1989; Bainbridge et al., 2012; Bruce et al., 2006; Cho & Azam, 1988; Cloern, 2001; Grossart & Simon, 1993). Although many sediment transport models have attempted to predict SPM dynamics, they mainly consider SPM to comprise only pure minerals (e.g., Delft3D, MIKE 21, and MIKE 3), while SPM in aquatic ecosystems also exists in a mixture with organic matter including living cells (Tang, 2017). The interactions between these constituents in biomineral SPM may cause changes in SPM dynamics as compared to mineral-only SPM. A better understanding of the implications of aggregate-attached biomass may therefore improve predictive models of sediment hydrodynamics and transport, as well as aid in determining scaling laws of large-scale morphodynamic processes in rivers and coastal zones (e.g., Seminara & Blondeaux, 2001). Together with the biomass assessment, mapping the spatial distribution of cells over individual SPM aggregates may be used to elaborate on possible mechanisms of cell dynamics including growth, mortality, attachment, and detachment and to develop models of cell colonization on mineral aggregates.

Growing attention has been paid to how SPM dynamics changes in the presence of a biological phase in addition to the mineral phase. The consistent finding throughout the recent literature is that although generally larger in size, biomineral aggregates are subject to higher drag and have lower excess density than mineral aggregates because of their lower capacity dimension, and thus, their settling velocity is not substantially different from mineral aggregates (Maggi, 2013, 2015; Maggi, Manning, & Winterwerp, 2006; Maggi & Tang, 2015; Shang et al., 2014; Tan et al., 2012; Tang & Maggi, 2016). It is noteworthy that earlier experiments have also shown a high variance in biomineral SPM geometric properties such as size L and capacity dimension d (Tang & Maggi, 2017), thus suggesting that the heterogeneity is particularly high relative to our current

knowledge of the interplay between biomass fraction and cell colonization patterns. One of the possible explanations for a high variance is the complexity of the multiple physical, chemical, and biological processes leading to the genesis of biomineral aggregates. These are initially formed by SPM aggregation in a sheared water environment. While mineral aggregation is mainly caused by electrochemical interactions, living cells can attach to mineral surfaces by secreting sticky substances like extracellular polymeric substances (EPSs) and transparent exopolymer particles (TEPs) (e.g., Alldredge, Passow, & Logan, 1993; Decho, 2000; Kiørboe, Andersen, & Dam, 1990). The presence of biological matter changes the shape and surface asperities of SPM substantially, and thus adds complexity to SPM aggregation as evidenced in both orthokinetic and perikinetic collision and aggregation (Tang, Alonso-Marroquin, & Maggi, 2014), or when aggregates trap cells and minerals carried by flow through the aggregates (e.g., Logan & Alldredge, 1989; Xiao et al., 2012). Once attached to minerals, living cells may colonize their environment by growing and interacting with other cells; other biological processes can also happen such as mortality, EPSs and TEPs secretion, and organic matter mineralization that can either enhance or hinder colonization progression (e.g., Grossart et al., 2006; Simon et al., 2002).

While cell growth and cell-cell interactions have widely been investigated for different microbes and environmental conditions (e.g., Gerbersdorf & Wieprecht, 2015; Goldschmidt, 2016; Grossart et al., 2003, 2006), colonization effects on biomineral aggregate geometry have received only a minor attention. Cell counting and visualization in biomineral SPM are often conducted through microscope imaging after staining cells with fluorochromes. However, cell visualization may be less effective when minerals mask cells and adsorb the dyes (e.g., Boenigk, 2004; Schallenberg, Kalff, & Rasmussen, 1989). Although cell counting may be improved through sample dilution and cell detachment methods (e.g., Boenigk, 2004; Gough & Stahl, 2003; Velji & Albright, 1986), the handling and processing of SPM aggregates can disrupt the aggregate structure, thus preventing the observation of cell spatial distributions and colonization patterns developing in a suspension.

This study introduces a novel method, OMCEC (optical measurement of cell colonization), to identify cell colonization patterns on individual SPM aggregates naturally settling through a water column. We aim to experimentally investigate (1) whether the carbon source concentration has an impact on cell colonization, (2) how cells colonize minerals, and (3) if a correlation between cell colonization patterns and aggregate geometry exists. In our experimental setup, stained montmorillonite minerals and *Saccharomyces cerevisiae*, a unicellular fungus commonly found in nutrient-rich waters and sediment (e.g., Bogusławska-Wąs & Dąbrowski, 2001; Hagler & Ahearn, 1987; Silva-Bedoya, Ramírez-Castrillón, & Osorio-Cadavid, 2014; Spencer and Spencer, 1997), were used as models for natural clays and microorganisms in aquatic ecosystems, respectively. The OMCEC method was first calibrated against mineral and biological SPM aggregates and, then, tested on incubations of *S. cerevisiae* and stained montmorillonite at four sucrose concentrations. Details of the OMCEC method, experimental procedures, data analyses, and results are presented in the following sections.

2. Methods

The OMCEC method combines of biochemical, optical, and computational techniques including mineral staining, cell incubation, settling column testing, and image acquisition and processing as detailed below.

2.1. Experimental Procedures, Samples, and Microparticle Image Velocimetry Acquisition

Fluorescent rhodamine B dye (Sigma Aldrich Inc., Australia) was used for mineral staining because its emission spectrum to visible light peaks at 580 nm and differs from that of microorganisms (i.e., 500 to 550 nm). It is easily adsorbed to minerals and is noncytotoxic at concentrations below 2 mg/L (Field et al., 1995; Giana et al., 2003; Hardy et al., 2016; Smart & Laidlaw, 1977). Montmorillonite was used because it has high cationic exchange capacity and large surface area (Bhattacharyya, SenGupta, & Sarma, 2014), which enhance dye adsorption.

Twelve grams of montmorillonite was stirred in 500 mL deionized water until homogeneous before adding 0.2 g rhodamine B powder (Figures 1a and 1b). This mixture was stirred for 3 h for the dye to adsorb. Next, stained minerals were let to settle, and the pink transparent supernatant was gradually withdrawn using a syringe (Figure 1c). The stained minerals were washed with water and naturally air-dried before being gently disaggregated and heated at 150°C for half an hour to inactivate microorganisms, if any (Figure 1d).
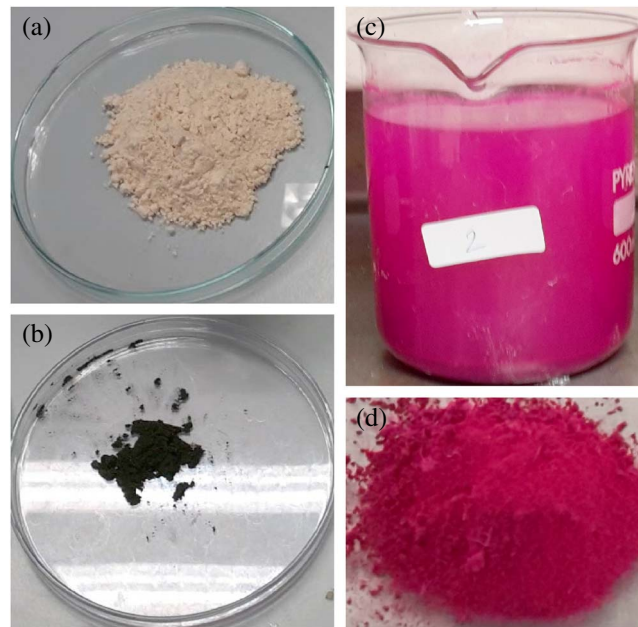
Figure 1. (a) Dry unstained montmorillonite, (b) rhodamine B powder, (c) supernatant with stained montmorillonite, (d) dry stained montmorillonite after washing and drying.

Four types of samples were prepared: unstained montmorillonite (M), stained montmorillonite (RM), *S. cerevisiae* (Y), and a biomineral mixture (RMY) of the previous two (Table 1). The M, RM, and RMY suspensions had a mineral concentration of 0.6 g/L, while the initial *S. cerevisiae* concentration in the RMY and Y samples was 0.17 g-dry/L. Four RMY samples were prepared with 0.6, 1.2, 2.4, and 4.8 g/L of sucrose, whereas one Y sample was prepared with 4.8 g/L sucrose and 0.001 g/L rhodamine B to replicate the rhodamine B release in RMY samples (Table 1). This rhodamine B concentration was measured using a 721G visible spectrophotometer. Y and RMY samples were then incubated at 30°C for 100 h in a climatic chamber (MLR-352H-PE, Panasonic) and were gently stirred three times per day to enhance sucrose accessibility by cells (Table 1).

Seven suspensions were tested in the settling column detailed in Tang and Maggi (2015a, 2016) (Table 1). SPM was gently transferred with a wide mouth pipette into the measuring section of the settling column and allowed to settle freely into the camera view. Settling SPM was illuminated by a thin light sheet generated by a 3.7 W, 400 lumens, cool white Cree LED transmitted through a system of optic fibers while SPM images were captured using a full-color CCD camera (Prosilica GT3400C) equipped with a high magnification lens (Navitar 12X Body Tube). The CCD sensor is made of 3384-by-2704 pixels and has a frequency of 3.054 frames per second in 8 bit depth and 4 bytes per pixel mode. The field of view was 6.67-by-5.23 mm, and the pixel size was 1.97-by-1.93 μm.

Table 1
Specifications of Suspension Types Used for Calibration and Testing

	Suspension type	Minerals (g/L)	*S. cerevisiae* (g-dry/L)	Sucrose (g/L)	Rhodamine B (g/L)	Sucrose/dry-biomass (g/g)
1		2	3	4	5	6
M	Unstained montmorillonite	0.60	–	–	–	–
RM	Stained montmorillonite	0.60	–	–	–	–
Y[a]	*S. cerevisiae*	–	0.17	4.80	0.001	28
RMY[a]	Stained montmorillonite	0.60	0.17	0.60		3.5
	and *S. cerevisiae*	0.60	0.17	1.20		7
		0.60	0.17	2.40		14
		0.60	0.17	4.80		28

[a]Incubated samples.

(a) Pre-processing

Raw full-color images

1. Multiply R_p, G_p by ten, set $B_p = 0$

2. Apply FFT filtering

3. Filter low intensity pixels

4. Remove isolated pixels

5. Extract individual aggregate images

6. Eliminate unfocused aggregate images

7. Normalize intensity of each image to 255 (Max (R_p, G_p) of all pixels in each image is 255)

Pre-processed aggregate images

(b) Post-processing

Pre-processed aggregate images

1. Normalize intensity of each pixel to 255 (Max (R_p, G_p) of each pixel in each image is 255)

2. Apply a threshold function to classify minerals and biomass

3. Correct error pixels on the left (if error conditions are satisfied)

4. Change isolated pixels of one phase to the other phase
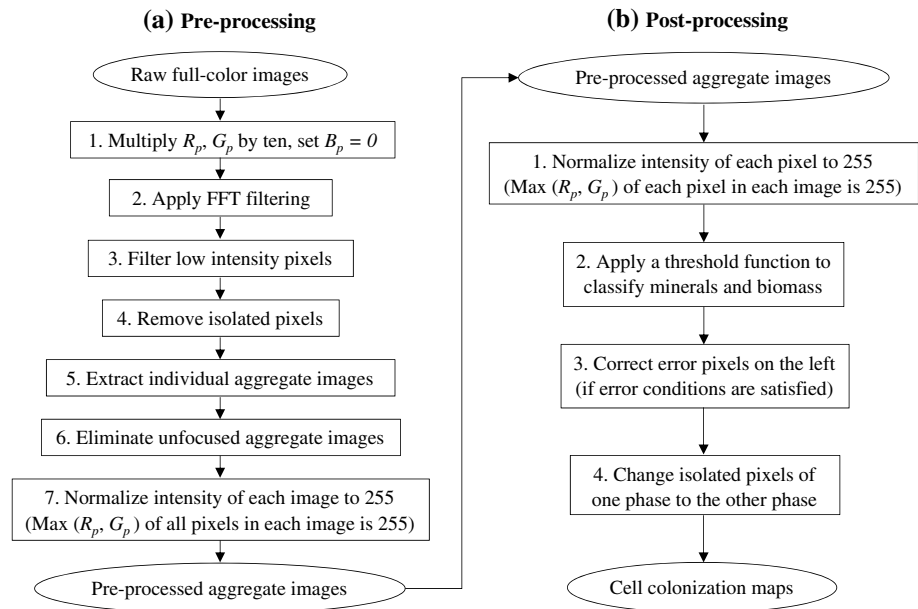
Cell colonization maps

Figure 2. Flowcharts for (a) image preprocessing and (b) postprocessing.

2.2. Image Preprocessing and Postprocessing

Full-color images were processed to remove noise and isolate aggregates from the background (Figure 2a). Each image pixel was defined by (R_p, G_p, B_p) intensities (red, green, and blue). The (R_p, G_p) channels were first amplified, while B_p was set to zero because the emission wavelengths of both materials are beyond the blue spectrum. A fast Fourier transform filter was next applied to remove high-frequency background noise in the (R_p, G_p) channels before a threshold was used to eliminate low-intensity pixels. Isolated pixels were considered noise and were removed because a single pixel area in our microparticle image velocimetry (μPIV) system was smaller than that of a montmorillonite particle and an *S. cerevisiae* cell. Individual aggregate images were extracted from the whole images using an image recognition algorithm (Maggi, 2007), and only in-focus images were chosen. Among various methods like artificial neural networks (e.g., MacDonald & Mullarney, 2015), we used the gray level local variance method (e.g., Pech-Pacheco et al., 2000; Pertuz, Puig, & Garcia, 2013) where an image with high-intensity gradients (i.e., larger than 2000) was considered in-focus. Finally, image intensities were normalized to 255 using $R_p^{'} = 255 R_p / I_p$ and $G_p^{'} = 255 G_p / I_p$, where $I_p = \max(R_1, \ldots, R_N, G_1, \ldots, G_N)$ is the maximum pixel intensity and N is the total pixel count in an image.

All pixels of RM and Y preprocessed images were scattered in the (R_p, G_p) space to classify whether they belonged to the mineral or the biomass phases. The 99% confidence lines were then determined (see the red and green lines in Figure 3a), and the bisector of the angle formed by the two lines was defined as

$$G_t = aR_p + b, \tag{1}$$

and was used as the threshold green intensity G_t at each R_p intensity, while $a = 0.564$ and $b = 1.190$ in equation (1) were known from the confidence limit lines (see the black line in Figure 3a). A pixel was attributed to the biomass phase if $G_p > G_t$ or to the mineral phase if $G_p \leq G_t$. Isolated pixels of one phase were changed into the other phase because single pixels were considered noise as in the preprocessing.

The OMCEC method was calibrated using equation (1) against RM and Y samples with the expectation that all pixels in RM (stained montmorillonite only) would be classified as minerals, and all pixels in Y (cells only) would be classified as biomass. Calibration results returned average errors of 7.25% and 4.70% in RM and Y samples, respectively, which were caused by pixels falling between the two confidence limits and by directional light source; i.e., the light sheet was shined onto the left side of the aggregates (Figures 3a and 3b).
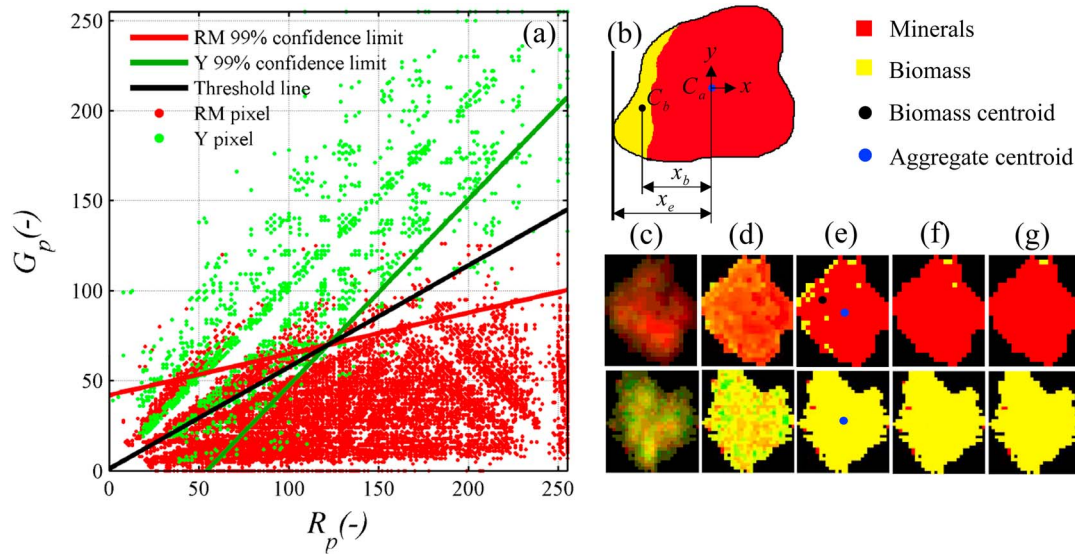
Figure 3. (a) Thresholding graph; pixels above and below the threshold were classified as biomass and minerals, respectively. (b) Conceptual representation of an RM aggregate image of the calibration set affected by the nonuniform illumination. (first row) RM aggregate images and (second row) Y aggregate images throughout the postprocessing as in Figure 2b: (c) after preprocessing, (d) after pixel normalization, (e) after phase thresholding, (f) after correction of nonuniform illumination, and (g) after changing isolated pixels. RM and Y stand for stained montmorillonite and *S. cerevisiae*, respectively.

To correct the first effect, the $\max(R_p, G_p)$ of each pixel of a preprocessed image was first normalized to 255 and the $\min(R_p, G_p)$ to $255 \min(R_p, G_p)/ \max(R_p, G_p)$. Application of this normalization (Figure 2b) redistributed some ambiguous pixels away or across the threshold, reduced the error in the Y sample to 3.57%, and slightly increased the error in the RM sample to 7.40%; because the overall improvement, the correction method was used in our analyses.

To correct the second effect, a system of reference was located at the aggregate centroid C_a, and the horizontal distance x_b between C_a and the biomass centroids C_b was compared to the distance x_e between the left vertical tangent and C_a (Figure 3b). In 95.4% of the RM images, C_b was at the left of C_a, and the average ratio $x_b/x_e = 0.36$ was used as a criterion to reduce further the error on calibration images. All images were tested against condition $x_b/x_e \geq 0.36$; if satisfied, a number equal to $\min(0.074N, N^*)$ of biomass pixels on the left side of the aggregate would be converted to mineral pixels, where N is the total pixel count and N^* is the total biomass pixel count on the left side of the aggregate. Applying this correction between steps 2 and 4 of the postprocessing (Figure 2b) reduced the error in the RM sample to 5.03% and did not have effects on the Y sample (see examples in Figures 3c to 3g).

2.3. Data Analyses and Cell Colonization Pattern Classification

Cell colonization maps were analyzed to retrieve the aggregate biomass and mineral fractions f_b and f_m as

$$f_b = \frac{m_b}{m_b + m_m}, \quad f_m = \frac{m_m}{m_b + m_m}, \tag{2}$$

where $m_b = A_b\rho_b$ and $m_m = A_m\rho_m$ are the wet biomass and mineral mass, respectively; A_b and A_m are the total pixel area of biomass and minerals, with the aggregate area $A = A_b + A_m$; $\rho_b = 1.1126$ g/cm^3 is the *S. cerevisiae* density (Baldwin & Kubitschek, 1984); and $\rho_m = 1.47$ g/cm^3 is the montmorillonite density at 100% hydration (De Wit & Arens, 1950). The linear aggregate size L was calculated as the length of the minimum square covering the aggregate image (Maggi & Winterwerp, 2004), while the aggregate three-dimensional capacity dimension d was estimated using the light intensity spectrum method (Tang & Maggi, 2015b). The scaling law for the fractal dimension d (Maggi, 2007)

$$d = \delta\left(\frac{L}{L_p}\right)^{\gamma}, \tag{3}$$

was used to retrieve the capacity dimension and size of the primary particles δ and L_p, as well as the characteristic parameter γ.

The average three-dimensional capacity dimension d_b of N_c cell clusters in an aggregate was determined as

$$d_b = \frac{1}{\sum\limits_{i=1}^{N_c} a_{b,i}} \sum_{i=1}^{N_c} d_{b,i} a_{b,i},$$ (4)

where $d_{b,i}$ and $a_{b,i}$ are the capacity dimension and projected area of the cell cluster i, respectively.

The Euclidean distance between the centroids of biomass and mineral phases was described with the symbol D_{mb} and used for analyses described next.

The average projected area a_b of all cell clusters in an aggregate was calculated as

$$a_b = \frac{A_b}{N_c}.$$ (5)

The dispersion index I_b of the cell cluster area was defined as

$$I_b = \frac{s}{a_b},$$ (6)

where $s = \left(\sum\limits_{i=1}^{N_c} (a_{b,i} - a_b)^2 \right)^{1/2}$ is the standard deviation of cell cluster area. Cell clusters in an aggregate are considered to have a similar area if $I_b < 1$. The contact index I_c between cell and mineral clusters was calculated as

$$I_c = \frac{\ell_{mb}}{p_b},$$ (7)

where ℓ_{mb} is the number of cell cluster pixels in contact with mineral clusters and p_b is the entire inner and outer perimeter of all cell clusters. Using equations (2) and (5) to (7), we quantitatively identified three types of aggregates: mineral, $f_b \leq 0.05$; biomineral, $0.05 < f_b < 0.95$; and biological, $f_b \geq 0.95$ (Figure 4a). Biomineral aggregates were classified into three types of cell colonization patterns: scattered, $a_b/A \leq 0.05$ and $I_b < 1$; well touched, $I_c > 0.5$; and poorly touched, $I_c \leq 0.5$ (see examples in Figure 4b).

The probability of observing a colonization pattern in a specific range of a generic metric quantity x was determined as

$$P_{S,x} = \frac{n_{S,x}}{n_x}, P_{W,x} = \frac{n_{W,x}}{n_x}, P_{P,x} = \frac{n_{P,x}}{n_x},$$ (8)

where $n_{S,x}$, $n_{W,x}$, and $n_{P,x}$ are the counts of scattered, well-touched, and poorly-touched patterns in that range, respectively, while $n_x = n_{S,x} + n_{W,x} + n_{P,x}$ is the corresponding total count.

2.4. Microscope Images

Images of SPM aggregates acquired using a Motic® series BA310 microscope at 40X magnification were used for qualitative comparisons to those from the µPIV system. Throughout all the 800 microscope aggregate images obtained from the RMY samples (Figure 4b, third row), aggregate types and colonization patterns quantitatively classified in section 2.3 were consistently observed. Although a low concentration of rhodamine B was released from stained montmorillonite during rehydration (0.001 g/L), cells in RMY samples retained their natural chromatic features (see examples in Figure 4b).

3. Results

A total of 2747 maps were experimentally retrieved using OMCEC for the four cell-mineral samples (RMY) at various sucrose concentrations and were used for analyses of cell colonization on SPM aggregates in the following sections.
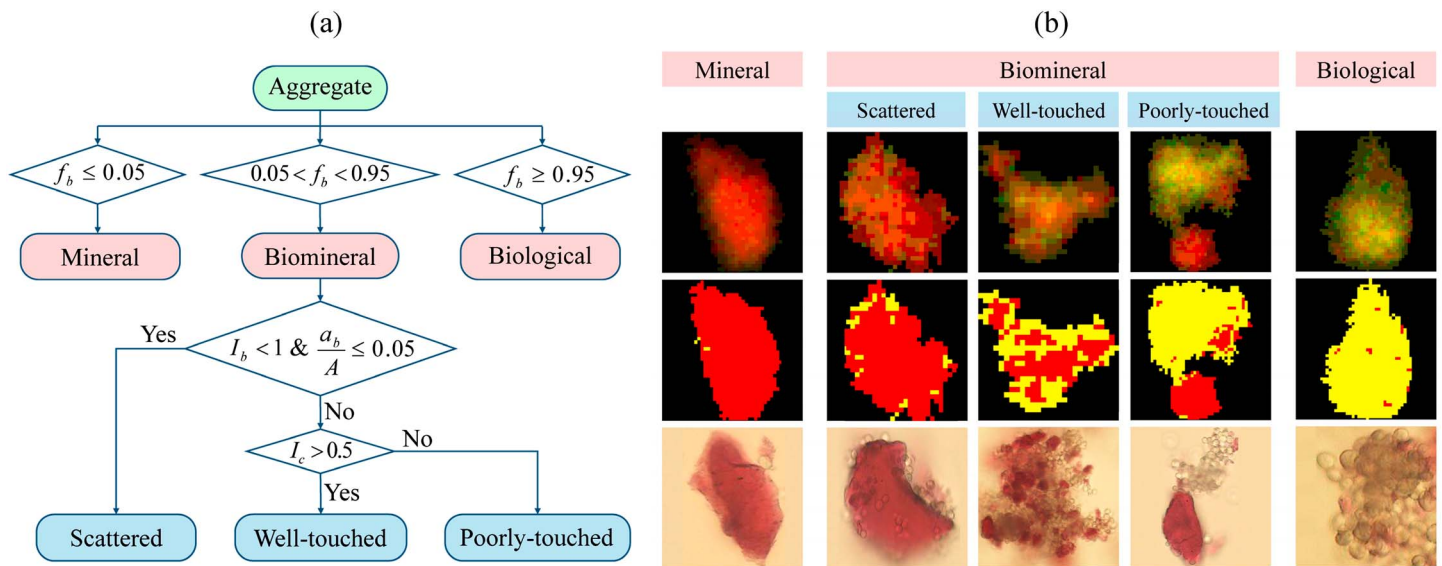
Figure 4. (a) Classification tree of aggregate types and cell colonization patterns. (b) Examples of classified aggregate types and cell colonization patterns; first, second, and third rows represent preprocessed images, colonization maps, and microscope images of similar aggregates for qualitative comparison, respectively; the red and yellow pixels in the second row represent minerals and cells, respectively.

3.1. Biomass Fraction and Sucrose Concentrations

The biomass fraction probability distribution peaked at $f_b \leq 0.1$ and $f_b > 0.9$, hence showing that aggregates prevalently mineral or biological are the most likely regardless of sucrose concentrations (Figure 5a).

The probability distribution of each aggregate type as a function of sucrose concentration shows that mineral aggregates were the most likely found at 0.6 g/L sucrose concentration but became rare at 4.8 g/L (Figure 5b). On the other hand, the probability of observing biomineral aggregates almost doubled with increasing sucrose concentration, while biological aggregates remained the least likely. These observations suggest that *S. cerevisiae* may have a greater preference for attaching to minerals than forming cell clusters when the concentration of a carbon source (sucrose) increased, or that the colonization rate increased, or both.

Contrary to our expectations, we did not find significant correlations between sucrose concentrations and colonization patterns because $P_{S, \text{[sucrose]}}$, $P_{W, \text{[sucrose]}}$, and $P_{P, \text{[sucrose]}}$ calculated using equation (8) were nearly invariant (Figure 5c). Given this observation, colonization maps of the RMY samples at the four sucrose concentrations were combined as one data set for the following analyses.

3.2. Biomass Fraction and Cell Colonization Patterns

Colonization maps of 1294 biomineral aggregates were analyzed, and a positive correlation between L and f_b was significant for large aggregates. While scattered and poorly-touched patterns occurred mostly in $f_b \leq 0.2$ and $f_b > 0.8$, respectively, well-touched patterns were observed throughout the entire f_b range and were predominant in $0.2 < f_b \leq 0.8$ (Figure 6a). An increasing attachment of small cell clusters to aggregates was observed with increasing f_b for the scattered pattern, but with cell clusters becoming larger and fewer for the other patterns (Figures 6b and 6c). Although the biomass and mineral phases became closer to each other as f_b increased, their distance in a poorly-touched pattern was always much greater than in the other patterns (Figure 6d).

3.3. Cell Colonization Mechanisms

If an increase in f_b is considered a proxy for cell colonization (Figure 6a), we can infer a colonization evolution that progresses from scattered to well-touched, and then to poorly-touched patterns. This transition, together with the correlation of $\overline{N_c}$, $\overline{a_b/A}$, and $\overline{D_{mb}/L}$ with f_b (Figures 6b to 6d), was instrumental in elaborating on the colonization mechanisms conceptually presented in Figure 6e and described below.
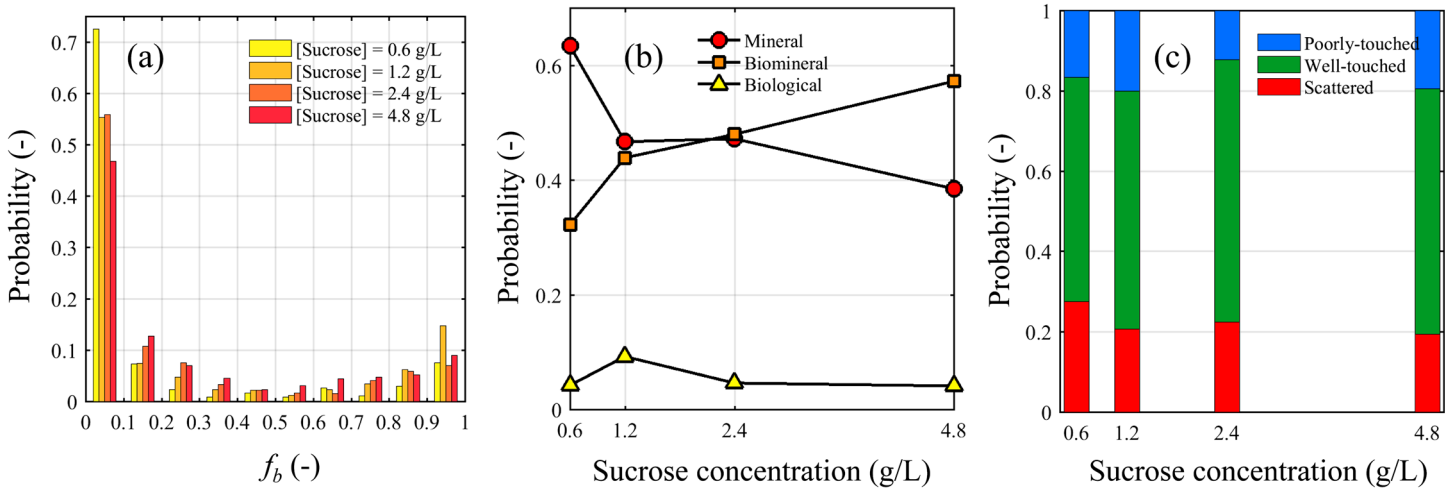
Figure 5. (a) Probability distribution of f_b in RMY samples. (b) Probability of observing mineral, biomineral, and biological aggregates against sucrose concentrations. (c) Cumulative probability of observing colonization patterns against sucrose concentrations. RMY stands for a mixture of stained montmorillonite and *S. cerevisiae*.

Cell colonization may begin with the attachment of small cell clusters to minerals, as suggested by a large $\overline{N_c}$ and low $\overline{a_b/A}$ when f_b is small (Figures 6b and 6c). Large cell clusters may also attach to minerals and form a poorly-touched pattern because very high $\overline{D_{mb}/L}$ was observed when $f_b \leq 0.6$ (Figure 6d, blue markers). Newly attached cell clusters are likely to join by unipolar cell budding as observed in young *S. cerevisiae* clusters (Vopálenská et al., 2010), while they tend to grow apart from each other when old (Palkova et al., 1997). Next, colonization may continue due to cell growth, with a preference for cell expansion on mineral surfaces because minerals provide the environment for microbial metabolism as a result of nutrient adsorption. This preference for mineral surfaces is reflected in a positive correlation between L and f_b in large aggregates and in the decline of $\overline{D_{mb}/L}$ (Figure 6d), indicating that biomass and mineral phases get closer to each other as f_b increases. Cell expansion is presumed to continue until the entire mineral is completely colonized. However, the larger the mineral surface covered by cells, the shorter the contact length between cell and mineral clusters remains, and thus aggregates characterized by a well-touched pattern may become poorly touched when f_b increases. Although cell attachment can also happen during the later stages of cell colonization (e.g., $\overline{N_c}$ increased with $\overline{a_b/A}$ being constant for the scattered pattern), cell growth and joining are the dominant mechanisms because a significant decrease and increase in $\overline{N_c}$ and $\overline{a_b/A}$ against f_b, respectively, was observed for the well-touched and poorly-touched patterns (Figures 6b and 6c).

In summary, analysis of colonization patterns may be used to infer colonization mechanisms. The scattered pattern occurs as a result of small cell cluster attachment while the well-touched pattern mainly occurs as a result of cell joining and growth on mineral surfaces. The poorly-touched pattern may be formed by two mechanisms: attachment of large cell clusters to minerals and growth of large cell clusters, with the latter starting either as a poorly-touched or a well-touched pattern.

3.4. Cell Colonization Patterns and Aggregate Geometry

Well-touched patterns were mainly observed to have low d_b values, while the others were mostly seen in high d_b ranges (Figure 7a). $P_{S,d}$ and $P_{P,d}$ calculated using equation (8) slightly increased and decreased, respectively, whereas $P_{W,d}$ remained stable with increasing d values (Figure 7b). The scattered pattern was only seen in small L ranges, $P_{W,L}$ nonlinearly increased, and $P_{P,L}$ was almost constant as L increased (Figure 7c).

Bin-averaged $\overline{d}$ values were mostly larger than 2.4 and decreased with increasing L_i regardless of patterns (Figure 7d), and the scaling law in equation (3) shows that the characteristic parameter γ was always negative. The primary particle size L_p ranged between 5 and 9 μm, which are the typical cell and mineral particle sizes. The primary particle capacity dimension was nearly invariant across the patterns and was relatively high, reflecting a compact structure of primary particles.
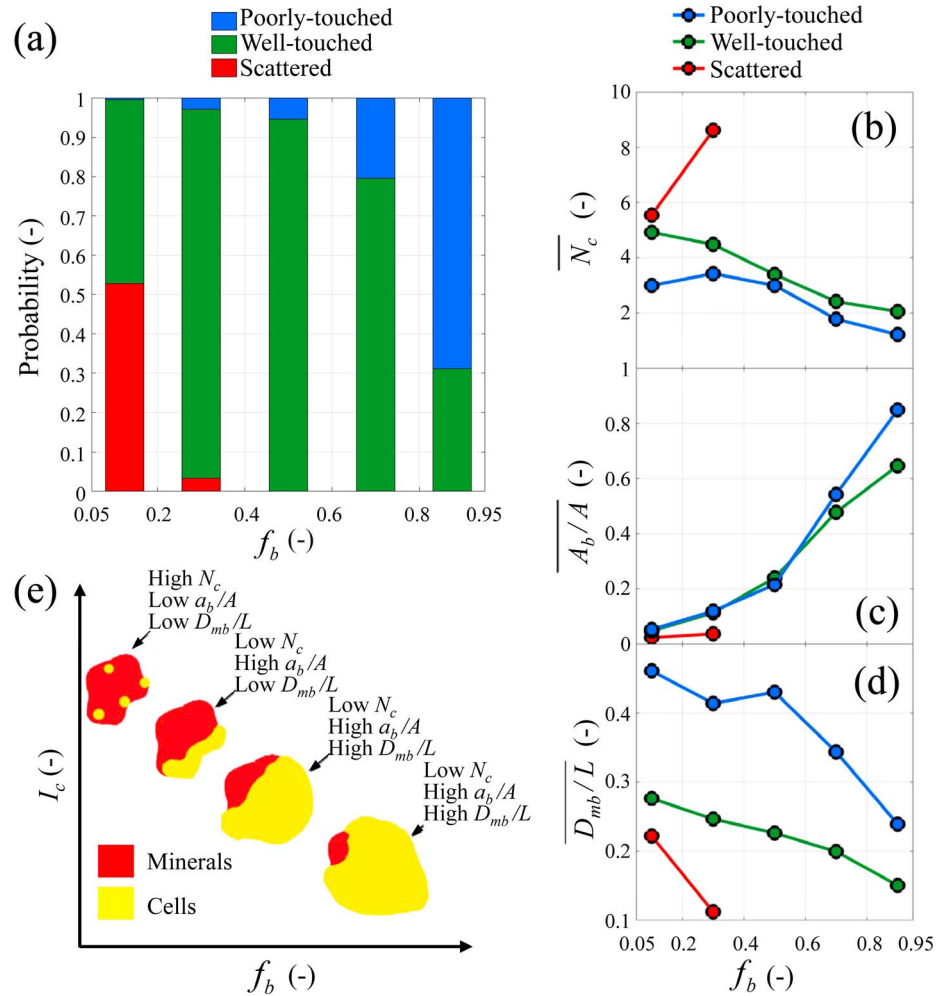
Figure 6. (a) Probability of observing colonization patterns against biomass fraction f_b. Bin-averaged (b) cell cluster count $\overline{N_c}$, (c) cell cluster area over aggregate area $\overline{a_b/A}$, and (d) centroid distance over aggregate size $\overline{D_{mb}/L}$ for colonization patterns against f_b, respectively. (e) Conceptual elaboration of cell colonization mechanisms.

The $\overline{d_b}$ values were high and almost constant against d for the scattered pattern but were positively corre-lated with d for the well-touched and poorly-touched patterns (Figure 7e). Because small cell clusters in the scattered pattern were always compact, a stochastic attachment of cell clusters may have had a stronger effect on d than $\overline{d_b}$. Figure 7f shows that $\overline{N_c}$ increased nearly linearly with increasing L_i for all patterns, but with slopes that differed from each other. The increasing $\overline{N_c}$ with L_i may be due to larger aggregates having larger surface area for cell attachment, and a lower slope suggests that cell growth plays a more important role in increasing L_i than facilitating cell attachment in the well-touched and poorly-touched patterns. Analysis of variance rejects the null hypothesis that a geometric property among d_b, d, L, and N_c is invariant against the tested range of another geometric property (i.e., significance $p < 0.001$), suggesting that the correlations observed in Figures 7d to 7f were significant.

4. Discussion

The OMCEC method is a promising approach for optical analyses of cell colonization on individual SPM aggregates because it preserves the aggregate structure and can be operated systematically, assuring objec-tive results, and reducing manual labor. OMCEC is based on PIV methods, and hence particle tracking and velocimetry can be coupled to biomass-to-mineral fraction analyses and widened to SPM aggregate hydrodynamics.
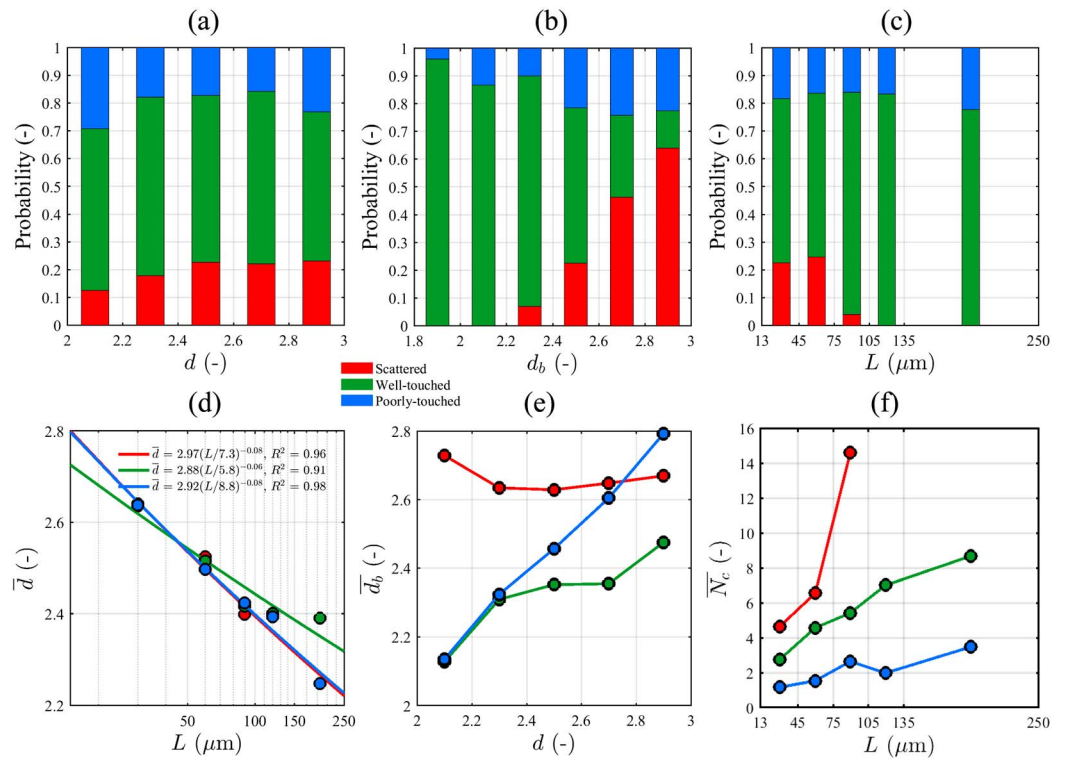
Figure 7. Probability of observing scattered, well-touched, and poorly touched patterns against (a) biomass phase capacity dimension d_b, (b) aggregate capacity dimension d, and (c) aggregate size L. Bin-averaged (d) $\overline{d}$ against L, (e) $\overline{d_b}$ against d, and (f) $\overline{N_c}$ against L for the three patterns. The lines in Figure 7d illustrate scaling function for bin-averaged $\overline{d}$ and L following equation (3), with the correlation coefficient R^2 representing the goodness of fit of equation (3) against given data.

The OMCEC method can be widely applied to laboratory experiments, but its in situ application may be limited because it requires mineral staining. The experimental setup in this study is a pilot test simplified with aggregates consisting of only one type of minerals and microorganisms, while aggregates in natural waters may comprise various microbial species such as bacteria, diatoms, and green algae, and other organic matter like debris and detritus. However, OMCEC is a framework with many adjustable submethods as described in section 2. Users can analyze more complex aggregates by incubating, for example, multiple microbial species or biological matter from natural waters, as long as the emission wavelengths of the biological matter are lower than 550 nm. Rhodamine B released in incubation samples is unlikely to affect natural chromatic features of any microorganism because this fluorescent dye has been shown to stain only the mitochondria (e.g., Johnson, Walsh, & Chen, 1980; Reungpatthanaphong et al., 2003; Scaduto & Grotyohann, 1999), which are not detectable in a PIV system at current camera resolutions. If microorganisms with emission wavelengths higher than 550 nm are used, other fluorescent dyes with emission wavelengths lower than 550 nm and compatible with minerals (e.g., fluorescein; Diaz et al., 2013) can be used.

SPM smaller than 15 μm were not captured in this study although the image pixel size was 1.97-by-1.93 μm likely because the fluorescence intensity was not high enough for the CCD sensor. Optics can be improved by an enhanced illumination system. An excitation wavelength about 530 nm combined with a 560 nm long-pass emission filter is often used to obtain the fluorescence of rhodamine B without other reflection wavelengths (e.g., Diaz et al., 2013; Hardy et al., 2016). However, this technique would prohibit the detection of cell fluorescence in the 500 to 550 nm bandwidth. Specifically to our setup, a visible white light spectrum was used without filters, and consequently, scattered light from SPM aggregates can be both the fluorescence and the reflected light. This uncertainty may be one of the explanations of why some pixels of the calibration set fell between the two confidence limits in Figure 3a. To eliminate this uncertainty as an alternative to our correction methods (see steps 1 and 3 in Figure 2b), a high-intensity excitation light at a wavelength shorter than 500 nm may be used with a 500 nm long-pass emission filter. In addition, the excitation light source can also be installed from multiple directions to provide a uniform illumination.

Overlaid cells and minerals impose a limit on this OMCEC method as much as in other microscope-based methods discussed in section 1. While cells overlaid by minerals were not detectable and did not affect the mineral fluorescence, cells laying onto mineral surfaces fluoresced at wavelengths between those of stained minerals and cells; thus, this may be another explanation for the pixels falling between the two confidence limits. Overlaying can be quantified using the microtome technique (e.g., Li & Ganczarczyk, 1990), micro-computed tomography scanning (e.g., Schmidt et al., 2015; Tisato et al., 2015), and focused ion beam nanotomography (Wheatland, Bushby, & Spencer, 2017); however, aggregates have to be fixed in a solid matrix for sampling and may experience substantial perturbation during sample preparation, and thus, coupling these techniques to the OMCEC method requires further consideration. Additionally, an aggregate image obtained in this OMCEC method is a 2-D projection of a complex 3-D aggregate, and thus, a potential development of OMCEC could include the use of the stereoscopic PIV and tomographic PIV methods (e.g., Elsinga et al., 2006; Jeon & Sung, 2012; Prasad, 2000).

The capacity dimension d_b of cell clusters in the scattered and poorly touched patterns (i.e., mainly in the range of 2.4 to 3; Figure 7a) matches experiments with pure *S. cerevisiae* aggregates, i.e., $d = 2.66 \pm 0.34$ (Logan & Wilkinson, 1991), and is higher than d_b for the well-touched pattern. This observation may imply that cell clusters in the first two patterns were formed either before colonizing minerals or when the colonization was nearly completed, while cell clusters in the well-touched pattern were the results of cell expansion on mineral surfaces.

Biomineral aggregates in this study were found to have relatively high $\overline{d}$ values (Figure 7d) as compared to those sampled in the field, i.e., 2.1 to 2.4 (Lartiges et al., 2001; Maggi & Tang, 2015) and activated sludge, i.e., 1.76 and 1.99 (Gorczyca & Ganczarczyk, 1996; Li & Leung, 2005). An explanation for the high d values is that no organic matter was tested in our system, excluding *S. cerevisiae* cells. It is noteworthy that *S. cerevisiae* cells are ellipsoid-shaped and adhere together or to minerals by their membrane stickiness (Verstrepen & Klis, 2006), and thus, they tend to form more compact clusters than those formed by bacteria in the same conditions (Logan & Wilkinson, 1991), and we infer that they also form compact biomineral aggregates.

On the one hand, our observations of cell attachment may be approximated by cluster-cluster aggregation kinetic models (e.g., Lin et al., 1989; Meakin, 1988; Schaefer, 1989; Weitz et al., 1985), in which clusters are randomly brought together via diffusion with the hypothesis that collision always leads to aggregation. Aggregates formed by this kinetics are often found to have d of about 1.8, which is smaller than d of the scattered pattern. The difference in d values is likely because cell clusters are smaller than mineral clusters, and thus, the diffusion limited particle-cluster aggregation model with d being around 2.52 (Meakin, 1988; Witten & Sander, 1981) may provide a better description to cell attachment mechanism in this study. On the other hand, microbial growth dynamics is often described by Eden's model (e.g., Eden, 1961; Richardson, 1973; Waclaw et al., 2015), in which an unoccupied neighbor site is chosen randomly and then filled by another particle (a cell in this case). This model seems to generate aggregates with very compact structures (Meakin, 1988) but may not be able to fully describe well-touched patterns, because the cell growth direction is subjectively decided, which is toward or apart from other cell clusters depending on their maturity, and toward minerals. The formation of biomineral aggregates is a combination of different kinetics and therefore may require the development of a model that can comprehensively take into account all these aggregation mechanisms.

Scattered patterns occurred by cell attachment at the early stages of cell colonization (Figures 6a to 6c), and thus, this mechanism was strongly correlated with the aggregate size L_i (Figure 7f), corroborating findings in Kiørboe et al. (2002). In addition, we found that the well-touched and poorly-touched patterns were predominant at the later stages of cell colonization (Figure 6a) and their $\overline{N_c}$-to-L_i ratios were lower than in scattered patterns (Figure 7f). These findings align with Kiørboe et al. (2002) and Grossart et al. (2003), in which cell-cell interactions increase the cell abundance (i.e., leading to an increasing L_i) much more than attachment. The positive correlation between L_i and cell counts was found in Kiørboe (2003), Knoll, Zwisler, and Simon (2001), and Passow and Alldredge (1994). On the other hand, Lartiges et al. (2001) suggest that L_i of biomineral aggregates is controlled by physical aggregation. However, this conclusion was drawn without considering the heterogeneity of the biological processes that happen during biomineral aggregate formation. Therefore, further investigation should be conducted to study simultaneous effects of cell colonization and aggregate-aggregate interactions to provide a better understanding of biomineral aggregate formation.

5. Conclusions

The OMCEC method has been described and tested to map cell colonization patterns on individual SPM aggregates. Applications of OMCEC suggested that the increase of a carbon source concentration in a model SPM suspension enhances cell colonization on minerals. Three cell colonization patterns have been quantitatively and qualitatively identified: scattered, well touched, and poorly touched, with the well-touched pattern being predominant. A correlation between the colonization patterns and biomass fraction was observed, which may imply an evolution of colonization mechanisms spanning from cell attachment to minerals, cell joining, and expansive growth on the mineral surface until the entire aggregate is colonized. The cell-mineral contact, on the one hand, significantly loosens cell cluster structure and, on the other hand, leads to the formation of dense SPM aggregates. The OMCEC method has been shown as a powerful tool for laboratory-scale studies, especially in relating SPM biophysical interactions to its hydrodynamics. Further applications of the OMCEC method to more complex systems could provide a better understanding of these small-scale interactions and their effects on large-scale processes in natural waters.

References

Alldredge, A. L., & Gotschalk, C. C. (1989). Direct observations of the mass flocculation of diatom blooms: Characteristics, settling velocities and formation of diatom aggregates. *Deep-Sea Research. Part I, Oceanographic Research Papers*, 36(2), 159–171. https://doi.org/10.1016/0198-0149(89)90131-3

Alldredge, A. L., Passow, U., & Logan, B. E. (1993). The abundance and significance of a class of large, transparent organic particles in the ocean. *Deep-Sea Research. Part I, Oceanographic Research Papers*, 40(6), 1131–1140. https://doi.org/10.1016/0967-0637(93)90129-Q

Bainbridge, Z. T., Wolanski, E., Álvarez-Romero, J. G., Lewis, S. E., & Brodie, J. E. (2012). Fine sediment and nutrient dynamics related to particle size and floc formation in a Burdekin River flood plume, Australia. *Marine Pollution Bulletin*, 65(4), 236–248. https://doi.org/10.1016/j.marpolbul.2012.01.043

Baldwin, W. W., & Kubitschek, H. E. (1984). Buoyant density variation during the cell cycle of Saccharomyces cerevisiae. *Journal of Bacteriology*, 158(2), 701–704.

Bhattacharyya, K. G., SenGupta, S., & Sarma, G. K. (2014). Interactions of the dye, Rhodamine B with kaolinite and montmorillonite in water. *Applied Clay Science*, 99, 7–17. https://doi.org/10.1016/j.clay.2014.07.012

Boenigk, J. (2004). A disintegration method for direct counting of bacteria in clay-dominated sediments: Dissolving silicates and subsequent fluorescent staining of bacteria. *Journal of Microbiological Methods*, 56(2), 151–159. https://doi.org/10.1016/j.mimet.2003.10.004

Bogusławska-Wąs, E., & Dąbrowski, W. (2001). The seasonal variability of yeasts and yeast-like organisms in water and bottom sediment of the Szczecin Lagoon. *International Journal of Hygiene and Environmental Health*, 203(5–6), 451–458. https://doi.org/10.1078/1438-4639-00056

Bruce, L. C., Hamilton, D., Imberger, J., Gal, G., Gophen, M., Zohary, T., & Hambright, K. D. (2006). A numerical simulation of the role of zooplankton in C, N and P cycling in Lake Kinneret, Israel. *Ecological Modelling*, 193(3–4), 412–436. https://doi.org/10.1016/j.ecolmodel.2005.09.008

Cho, B. C., & Azam, F. (1988). Major role of bacteria in biogeochemical fluxes in the ocean's interior. *Nature*, 332(6163), 441–443. https://doi.org/10.1038/332441a0

Cloern, J. E. (2001). Our evolving conceptual model of the coastal eutrophication problem. *Marine Ecology Progress Series*, 210, 223–253. https://doi.org/10.3354/meps210223

De Wit, C. T., & Arens, P. L. (1950), Moisture content and density of some clay minerals and some remarks on the hydration pattern of clay. Paper presented at 4th International Congress of Soil Science, Amsterdam, Netherlands.

Decho, A. W. (2000). Microbial biofilms in intertidal systems: An overview. *Continental Shelf Research*, 20(10), 1257–1273. https://doi.org/10.1016/S0278-4343(00)00022-4

Diaz, C. A., Xia, Y., Rubino, M., Auras, R., Jayaraman, K., & Hotchkiss, J. (2013). Fluorescent labeling and tracking of nanoclay. *Nanoscale*, 5(1), 164–168. https://doi.org/10.1039/C2NR32978F

Eden, M. (1961). A two-dimensional growth process. In J. Neyman (Ed.), *Proceedings of the fourth berkeley symposium on mathematical statistics and probability* (Vol. IV, pp. 223–239). Berkeley: University of California Press.

Elsinga, G. E., Scarano, F., Wieneke, B., & van Oudheusden, B. W. (2006). Tomographic particle image velocimetry. *Experiments in Fluids*, 41(6), 933–947. https://doi.org/10.1007/s00348-006-0212-z

Field, M. S., Wilhelm, R. G., Quinlan, J. F., & Aley, T. J. (1995). An assessment of the potential adverse properties of fluorescent tracer dyes used for groundwater tracing. *Environmental Monitoring and Assessment*, 38(1), 75–96. https://doi.org/10.1007/BF00547128

Gerbersdorf, S. U., & Wieprecht, S. (2015). Biostabilization of cohesive sediments: Revisiting the role of abiotic conditions, physiology and diversity of microbes, polymeric secretion, and biofilm architecture. *Geobiology*, 13(1), 68–97. https://doi.org/10.1111/gbi.12115

Giana, H. E., Silveira, L. Jr., Zângaro, R. A., & Pacheco, M. T. T. (2003). Rapid identification of bacterial species by fluorescence spectroscopy and classification through principal components analysis. *Journal of Fluorescence*, 13(6), 489–493. https://doi.org/10.1023/B:JOFL.0000008059.74052.3c

Goldschmidt, F. (2016). The role of metabolic interactions in spatial self-organization and diversity of expanding microbial communities, (PhD thesis). Department of Environmental Systems Science, ETH Zürich, Zürich, Switzerland. https://doi.org/10.3929/ethz-a-010669776

Gorczyca, B., & Ganczarczyk, J. (1996). Image analysis of alum coagulated mineral suspensions. *Environmental Technology*, 17(12), 1361–1369. https://doi.org/10.1080/09593331708616505

Gough, H. L., & Stahl, D. A. (2003). Optimization of direct cell counting in sediment. *Journal of Microbiological Methods*, 52(1), 39–46. https://doi.org/10.1016/S0167-7012(02)00135-5

Grossart, H. P., Kiørboe, T., Tang, K., & Ploug, H. (2003). Bacterial colonization of particles: Growth and interactions. *Applied and Environmental Microbiology*, 69(6), 3500–3509. https://doi.org/10.1128/AEM.69.6.3500-3509.2003

Grossart, H. P., Kiørboe, T., Tang, K. W., Allgaier, M., Yam, E. M., & Ploug, H. (2006). Interactions between marine snow and heterotrophic bacteria: Aggregate formation and microbial dynamics. *Aquatic Microbial Ecology*, 42, 19–26. https://doi.org/10.3354/ame042019

Grossart, H. P., & Simon, M. (1993). Limnetic macroscopic organic aggregates (lake snow): Occurrence, characteristics, and microbial dynamics in Lake Constance. *Limnology and Oceanography*, *38*(3), 532–546. https://doi.org/10.4319/lo.1993.38.3.0532

Hagler, A. N., & Ahearn, D. G. (1987). Ecology of aquatic yeasts. In A. H. Rose, & J. S. Harrison (Eds.), *The yeasts* (Vol. 1, pp. 181–205). London: Academic Press.

Hardy, R. A., Pates, J. M., Quinton, J. N., & Coogan, M. P. (2016). A novel fluorescent tracer for real-time tracing of clay transport over soil surfaces. *Catena*, *141*, 39–45. https://doi.org/10.1016/j.catena.2016.02.011

Jeon, Y. J., & Sung, H. J. (2012). Three-dimensional PIV measurement of flow around an arbitrarily moving body. *Experiments in Fluids*, *53*(4), 1057–1071. https://doi.org/10.1007/s00348-012-1350-0

Johnson, L. V., Walsh, M. L., & Chen, L. B. (1980). Localization of mitochondria in living cells with rhodamine 123. *Proceedings of the National Academy of Sciences of the United States of America*, *77*(2), 990–994.

Kiørboe, T. (2003). Marine snow microbial communities: Scaling of abundances with aggregate size. *Aquatic Microbial Ecology*, *33*, 67–75. https://doi.org/10.3354/ame033067

Kiørboe, T., Andersen, K. P., & Dam, H. G. (1990). Coagulation efficiency and aggregate formation in marine phytoplankton. *Marine Biology*, *107*(2), 235–245. https://doi.org/10.1007/BF01319822

Kiørboe, T., Grossart, H. P., Ploug, H., & Tang, K. (2002). Mechanisms and rates of bacterial colonization of sinking aggregates. *Applied and Environmental Microbiology*, *68*(8), 3996–4006. https://doi.org/10.1128/AEM.68.8.3996-4006.2002

Knoll, S., Zwisler, W., & Simon, M. (2001). Bacterial colonization of early stages of limnetic diatom microaggregates. *Aquatic Microbial Ecology*, *25*(2), 141–150. https://doi.org/10.3354/ame025141

Lartiges, B. S., Deneux-Mustin, S., Villemin, G., Mustin, C., Barres, O., Chamerois, M., … Babut, M. (2001). Composition, structure and size distribution of suspended particulates from the Rhine River. *Water Research*, *35*(3), 808–816. https://doi.org/10.1016/S0043-1354(00)00293-1

Li, D. H., & Ganczarczyk, J. J. (1990). Structure of activated sludge flocs. *Biotechnology and Bioengineering*, *35*(1), 57–65. https://doi.org/10.1002/bit.260350109

Li, X. Y., & Leung, R. P. C. (2005). Determination of the fractal dimension of microbial flocs from the change in their size distribution after breakage. *Environmental Science & Technology*, *39*(8), 2731–2735. https://doi.org/10.1021/es049177+

Lin, M. Y., Lindsay, H., Weitz, D. A., Ball, R. C., Klein, R., & Meakin, P. (1989). Universality in colloid aggregation. *Nature*, *339*, 360–362. https://doi.org/10.1038/339360a0

Logan, B. E., & Alldredge, A. L. (1989). Potential for increased nutrient uptake by flocculating diatoms. *Marine Biology*, *101*(4), 443–450. https://doi.org/10.1007/BF00541645

Logan, B. E., & Wilkinson, D. B. (1991). Fractal dimensions and porosities of Zoogloea ramigera and Saccharomyces cerevisiae aggregates. *Biotechnology and Bioengineering*, *38*(4), 389–396. https://doi.org/10.1002/bit.260380409

MacDonald, I. T., & Mullarney, J. C. (2015). A novel "FlocDrifter" platform for observing flocculation and turbulence processes in a lagrangian frame of reference. *Journal of Atmospheric and Oceanic Technology*, *32*(3), 547–561. https://doi.org/10.1175/JTECH-D-14-00106.1

Maggi, F. (2007). Variable fractal dimension: A major control for floc structure and flocculation kinematics of suspended cohesive sediment. *Journal of Geophysical Research*, *112*, C07012. https://doi.org/10.1029/2006JC003951

Maggi, F. (2013). The settling velocity of mineral, biomineral, and biological particles and aggregates in water. *Journal of Geophysical Research: Oceans*, *118*, 2118–2132. https://doi.org/10.1002/jgrc.20086

Maggi, F. (2015). Experimental evidence of how the fractal structure controls the hydrodynamic resistance on granular aggregates moving through water. *Journal of Hydrology*, *528*, 694–702. https://doi.org/10.1016/j.jhydrol.2015.07.002

Maggi, F., Manning, A. J., & Winterwerp, J. C. (2006). Image separation and geometric characterisation of mud flocs. *Journal of Hydrology*, *326*(1), 325–348. https://doi.org/10.1016/j.jhydrol.2005.11.005

Maggi, F., & Tang, F. H. M. (2015). Analysis of the effect of organic matter content on the architecture and sinking of sediment aggregates. *Marine Geology*, *363*, 102–111. https://doi.org/10.1016/j.margeo.2015.01.017

Maggi, F., & Winterwerp, J. C. (2004), Method for computing the three-dimensional capacity dimension from two-dimensional projections of fractal aggregates, *Physical Review E*, *69*(1), 011405. https://doi.org/10.1103/PhysRevE.69.011405.

Meakin, P. (1988). Fractal aggregates. *Advances in Colloid and Interface Science*, *28*, 249–331. https://doi.org/10.1016/0001-8686(87)80016-7

Palkova, Z., Janderova, B., Gabriel, J., & Zikanova, B. (1997). Ammonia mediates communication between yeast colonies. *Nature*, *390*(6659), 532–536.

Passow, U., & Alldredge, A. L. (1994). Distribution, size and bacterial colonization of transparent exopolymer particles (TEP) in the ocean. *Marine Ecology Progress Series*, *113*(1–2), 185–198. https://doi.org/10.3354/meps113185

Pech-Pacheco, J. L., Cristóbal, G., Chamorro-Martinez, J., & Fernández-Valdivia, J. (2000). Diatom autofocusing in brightfield microscopy: A comparative study. Paper presented at 15th International Conference on Pattern Recognition, IEEE (pp. 314–317). Barcelona, Spain.

Pertuz, S., Puig, D., & Garcia, M. A. (2013). Analysis of focus measure operators for shape-from-focus. *Pattern Recognition*, *46*(5), 1415–1432. https://doi.org/10.1016/j.patcog.2012.11.011

Prasad, A. K. (2000). Stereoscopic particle image velocimetry. *Experiments in Fluids*, *29*(2), 103–116. https://doi.org/10.1007/s003480000143

Reungpatthanaphong, P., Dechsupa, S., Meesungnoen, J., Loetchutinat, C., & Mankhetkorn, S. (2003). Rhodamine B as a mitochondrial probe for measurement and monitoring of mitochondrial membrane potential in drug-sensitive and-resistant cells. *Journal of Biochemical and Biophysical Methods*, *57*(1), 1–16. https://doi.org/10.1016/S0165-022X(03)00032-0

Richardson, D. (1973). Random growth in a tessellation. *Mathematical Proceedings of the Cambridge Philosophical Society*, *74*(3), 515–528. https://doi.org/10.1017/S0305004100077288

Scaduto, R. C., & Grotyohann, L. W. (1999). Measurement of mitochondrial membrane potential using fluorescent rhodamine derivatives. *Biophysical Journal*, *76*(1), 469–477. https://doi.org/10.1016/S0006-3495(99)77214-0

Schaefer, D. W. (1989). Polymers, fractals, and ceramic materials. *Science*, *243*(4894), 1023–1027.

Schallenberg, M., Kalff, J., & Rasmussen, J. B. (1989). Solutions to problems in enumerating sediment bacteria by direct counts. *Applied and Environmental Microbiology*, *55*(5), 1214–1219.

Schmidt, H., Vetterlein, D., Köhne, J. M., & Eickhorst, T. (2015). Negligible effect of X-ray μ-CT scanning on archaea and bacteria in an agricultural soil. *Soil Biology and Biochemistry*, *84*, 21–27. https://doi.org/10.1016/j.soilbio.2015.02.010

Seminara, G., & Blondeaux, P. (Eds) (2001). *River, coastal and estuarine morphodynamics*. Berlin: Springer Science & Business Media.

Shang, Q. Q., Fang, H. W., Zhao, H. M., He, G. J., & Cui, Z. H. (2014). Biofilm effects on size gradation, drag coefficient and settling velocity of sediment particles. *International Journal of Sediment Research*, *29*(4), 471–480. https://doi.org/10.1016/S1001-6279(14)60060-3

Silva-Bedoya, L. M., Ramírez-Castrillón, M., & Osorio-Cadavid, E. (2014). Yeast diversity associated to sediments and water from two Colombian artificial lakes. *Brazilian Journal of Microbiology*, *45*(1), 135–142. https://doi.org/10.1590/S1517-83822014005000035

Simon, M., Grossart, H. P., Schweitzer, B., & Ploug, H. (2002). Microbial ecology of organic aggregates in aquatic ecosystems. *Aquatic Microbial Ecology*, *28*(2), 175–211. https://doi.org/10.3354/ame028175

Smart, P. L., & Laidlaw, I. M. S. (1977). An evaluation of some fluorescent dyes for water tracing. *Water Resources Research*, *13*, 15–33. https://doi.org/10.1029/WR013i001p00015

Spencer, J. F. T., & Spencer, D. M. (Eds.) (1997). *Yeasts in natural and artificial habitats*. New York: Springer.

Tan, X. L., Zhang, G. P., Yin, H., Reed, A. H., & Furukawa, Y. (2012). Characterization of particle size and settling velocity of cohesive sediments affected by a neutral exopolymer. *International Journal of Sediment Research*, *27*(4), 473–485. https://doi.org/10.1016/S1001-6279(13)60006-2

Tang, F. H. M. (2017). Microbiological modulation of suspended particulate matter dynamics: A study of biological flocculation in nutrient-enriched waters, Ph.D. thesis, School of Civil Engineering, The Univ. of Sydney, Sydney, Australia.

Tang, F. H. M., Alonso-Marroquin, F., & Maggi, F. (2014). Stochastic collision and aggregation analysis of kaolinite in water through experiments and the spheropolygon theory. *Water Research*, *53*, 180–190. https://doi.org/10.1016/j.watres.2014.01.026

Tang, F. H. M., & Maggi, F. (2015a). A laboratory facility for flocculation-related experiments (Rep. R952), The University of Sydney, Sydney, Australia.

Tang, F. H. M., & Maggi, F. (2015b). Reconstructing the fractal dimension of granular aggregates from light intensity spectra. *Soft Matter*, *11*(47), 9150–9159. https://doi.org/10.1039/C5SM01885D

Tang, F. H. M., & Maggi, F. (2016). A mesocosm experiment of suspended particulate matter dynamics in nutrient- and biomass-affected waters. *Water Research*, *89*, 76–86. https://doi.org/10.1016/j.watres.2015.11.033

Tang, F. H. M., & Maggi, F. (2017). Living microorganisms change the information (Shannon) content of a geophysical system. *Scientific Reports*, *7*, 3320. https://doi.org/10.1038/s41598-017-03479-1

Tisato, N., Torriani, S. F. F., Monteux, S., Sauro, F., De Waele, J., Tavagna, M. L., … Bontognali, T. R. R. (2015). Microbial mediation of complex subterranean mineral structures. *Scientific Reports*, *5*, 15525. https://doi.org/10.1038/srep15525

Velji, M. I., & Albright, L. J. (1986). Microscopic enumeration of attached marine bacteria of seawater, marine sediment, fecal matter, and kelp blade samples following pyrophosphate and ultrasound treatments. *Canadian Journal of Microbiology*, *32*(2), 121–126. https://doi.org/10.1139/m86-024

Verstrepen, K. J., & Klis, F. M. (2006). Flocculation, adhesion and biofilm formation in yeasts. *Molecular Microbiology*, *60*(1), 5–15. https://doi.org/10.1111/j.1365-2958.2006.05072.x

Vopálenská, I., Šťovíček, V., Janderová, B., Váchová, L., & Palková, Z. (2010). Role of distinct dimorphic transitions in territory colonizing and formation of yeast colony architecture. *Environmental Microbiology*, *12*(1), 264–277. https://doi.org/10.1111/j.1462-2920.2009.02067.x

Waclaw, B., Bozic, I., Pittman, M. E., Hruban, R. H., Vogelstein, B., & Nowak, M. A. (2015). A spatial model predicts that dispersal and cell turnover limit intratumour heterogeneity. *Nature*, *525*(7568), 261. https://doi.org/10.1038/nature14971

Weitz, D. A., Huang, J. S., Lin, M. Y., & Sung, J. (1985). Limits of the fractal dimension for irreversible kinetic aggregation of gold colloids. *Physical Review Letters*, *54*(13), 1416. https://doi.org/10.1103/PhysRevLett.54.1416

Wheatland, J. A. T., Bushby, A. J., & Spencer, K. L. (2017). Quantifying the structure and composition of flocculated suspended particulate matter using focused ion beam nanotomography. *Environmental Science & Technology*. https://doi.org/10.1021/acs.est.7b00770

Witten, T. A. Jr., & Sander, L. M. (1981). Diffusion-limited aggregation, a kinetic critical phenomenon. *Physical Review Letters*, *47*(19), 1400. https://doi.org/10.1103/PhysRevLett.47.1400

Xiao, F., Li, X., Lam, K., & Wang, D. (2012). Investigation of the hydrodynamic behavior of diatom aggregates using particle image velocimetry. *Journal of Environmental Sciences*, *24*(7), 1157–1164. https://doi.org/10.1016/S1001-0742(11)60960-1